Analysis of the Eternaus Explorer Hydrogen Airship: Analytical and CFD Investigation at Sea-Level Conditions

Hans G. Kraus[1]

Innovair Creation, Development & Operation of Special Aircraft 1, São Paulo, São Paulo, Zip Code, Brazil

Felipe J. da Costa[2]

UNIVAP - Universidade do Vale do Paraíba 2, São José dos Campos, São Paulo, Zip Code, Brazil

Anderson Z. Nakazato[3] and Bruno C. Lima[4]

BRENG Engineering and Technology 2, 3 and 4, São José dos Campos, São Paulo, Zip Code, Brazil

This paper presents a combined analytical and numerical investigation of the external aerodynamic behavior of the Eternaus Explorer 16.9/100 H_2 airship, part of the broader Eternaus Project aiming to develop sustainable, large-scale hydrogen-lifted airships for multipurpose civil and defense applications. The Explorer model, 100 m in length and 16.9 m in maximum diameter, operates under a bidirectionally prestressed aluminum super-rigid hull that provides both structural lightness and aerodynamic efficiency. The study focuses on the boundary-layer development and external flow characteristics under sea-level conditions, using both analytical laminar and turbulent models and a 3D axisymmetric CFD simulation performed with ANSYS Fluent 2025 R2. The simulation employed a pressure-based transient solver, k–ω SST turbulence model with near-wall resolution ($y^+ < 1$), and approximately 7.7×10^5 quadrilateral elements. The results showed a predominantly attached flow, smooth pressure recovery near the tail, and a minor separation region consistent with slender-body theory predictions. Analytical results were compared against CFD-derived wall pressure and velocity distributions, showing strong agreement in boundary-layer thickness growth and skin friction coefficients. The study concludes that the Explorer configuration maintains aerodynamic stability and low viscous drag at operational cruise speeds (39-58 m/s).

I. Introduction

The Eternaus Project, Figure 1, aims to redefine the design paradigm of large hydrogen airships through the use of super-rigid hulls with bidirectional prestressing, combining lightweight aluminum alloys with high structural strength [1]. This configuration enables the construction of vessels capable of carrying 6,000–10,000 kg of payload with extremely low operating costs and unprecedented autonomy, up to 65,000 km per fuel cycle.

The Explorer model serves as the experimental and aerodynamic demonstrator for the Eternaus system. Its 100-meter-long, 16.9-meter-diameter hull is optimized for low drag and stable flight in low-to-medium Reynolds number

[1] CEO, Business Unit.

[2] Professor, Aeronautical and Space Engineering Department.

[3] Researcher, R, D&I Department.

[4] Engineer, Aerospace Research Department.

regimes (Re ≈ 4×10^7). Understanding its aerodynamic behavior is critical for scaling future models and for validating the structural coupling between the prestressed hull and external flow loads [2].

The present work combines a boundary-layer analytical analysis and a Computational Fluid Dynamics (CFD) study to evaluate the aerodynamic performance of the Explorer at sea level, focusing on laminar-turbulent transition, wall shear stress, and overall flow topology. The study uses the ANSYS Fluent 2025 R2 solver as the primary computational platform, integrating modern turbulence modeling techniques with empirical boundary-layer correlations [3,4].

The Eternaus Project aims to develop a family of large-scale airships intended for logistics, operational, environmental, and specialized transport applications. The design of these vehicles is based on rigid and pressurized structural solutions combined with modern engineering concepts, targeting high operational safety, versatility, and energy efficiency.

Within this family, the Explorer model (Figure 1) represents the smallest airship in the series and is adopted as the initial platform for technical evaluation. Due to its reduced dimensions compared to the other Eternaus models, the Explorer is particularly suitable for preliminary studies of physical, mathematical, and aerodynamic feasibility, serving as a reference for future analyses and for scaling solutions to larger aircraft.

This paper presents an external aerodynamic assessment of the Explorer airship, carried out through Computational Fluid Dynamics (CFD) simulations, with emphasis on the analysis of the flow around the geometry and the determination of the vehicle's overall drag coefficient.

Figure 1 – Eternaus Explorer Concept.

II. Vehicle Description and Operating Conditions

The Explorer 16.9/100 configuration features a smooth, axisymmetric body designed to minimize separation and form drag. The vehicle's structural and aerodynamic parameters are summarized below:

Parameter	**Symbol**	**Value**
Total length	L	100 m
Max diameter	D	16.9 m
Surface area	S	4,330 m²
Hull material	—	Al-2090-T83 sheet
Skin thickness	e	0.4 mm
Operational speed	V	58 m/s (≈210 km/h max) / 39 m/s (≈140 km/h max)
Gas	—	Hydrogen (internal), Air (external flow)
Pressure differential	Po	420 mmH_2O
Altitude	h	0 m (sea level)

At sea level (ρ = 1.225 kg/m³, μ = 1.789×10^{-5} kg/m·s), the characteristic Reynolds number is:

$$Re_L = \frac{\rho V L}{\mu} \approx 4.0 \times 10^7 \tag{1}$$

indicating a fully turbulent boundary layer for most of the hull, with potential laminar onset near the stagnation region [5,6].

III. Methodology

To carry out the Aerodynamic Analysis of the Explorer Airship, preliminary studies are considered necessary, taking into account Theoretical-Analytical Analysis, Theoretical-Numerical Simulation, and Mechanical Dimensional Design methodologies.

Computational codes are developed based on the Navier–Stokes equations to perform Theoretical-Numerical Simulations. In this context, numerical simulations were conducted using a professional license of the software *Fluent*, which combines the physics of Computational Fluid Dynamics (CFD) with years of expert development in CFD challenges, and is commercialized by ANSYS, Inc. Additionally, a comparison was carried out between the results obtained from the analytical analysis and the numerical simulation of the Explorer Airship.

It is important to highlight that the methodologies employed, in addition to considering entropy, must comply with the fundamental principles of physics, namely: the Principle of Conservation of Mass, the Principle of Linear Momentum, and the Principle of Conservation of Energy.

The quantification of these fundamental principles is performed through the formulation developed by Navier–Stokes [7], which is, a priori, valid for continuous media; transient flow; incompressible and/or compressible regimes; laminar and/or turbulent flows; neglecting body forces, volumetric heating, and mass diffusion; and may be described in two-dimensional Cartesian coordinates.

For the execution of the Aerodynamic Analysis of the Explorer Airship, preliminary studies are also required, considering general design methodologies and their respective components, in order to proceed with the following steps:

- Assist in project coordination: consult technical standards and company drawing guidelines; collaborate in defining project directives; request complementary designs; support project integration; participate in project review meetings; check designs under supervision; archive project-related documents;
- Plan project development: analyze designs; define work methodology; support engineers in feasibility studies; establish deadlines for project development;
- Research new product and process technologies applicable to the project: follow total quality principles; assess material feasibility; use specialized software such as *Autodesk Inventor*; apply compatible technologies that enhance the project's structural performance;
- Use CAD (Computer-Aided Design) tools for illustrative documentation of components.

A. Theoretical-Analytical Analysis

The governing equations known as the Navier–Stokes equations [8] are valid for a continuous medium, incompressible and/or compressible flow, laminar, two-dimensional, and unsteady (transient), neglecting body forces, volumetric heating, and mass diffusion. They can be described in Cartesian coordinates and in conservative form as:

$$\frac{\partial U}{\partial t} + \frac{\partial E}{\partial x} + \frac{\partial F}{\partial y} + \frac{\partial G}{\partial z} = 0 \tag{2}$$

where $U$is the solution vector, and E, F, and $G$are the column vectors of the flux terms, given by:

$$U = \begin{Bmatrix} \rho \\ \rho u \\ \rho v \\ \rho w \\ E_t \end{Bmatrix} \tag{3}$$

$$E = \begin{Bmatrix} \rho u \\ \rho u^2 + p - \tau_{xx} \\ \rho uv - \tau_{xy} \\ \rho uw - \tau_{xz} \\ (E_t + p)u + q_x - u\tau_{xx} - v\tau_{xy} - w\tau_{xz} \end{Bmatrix} \tag{4}$$

$$F = \begin{Bmatrix} \rho v \\ \rho vu - \tau_{yx} \\ \rho v^2 + p - \tau_{yy} \\ \rho vw - \tau_{yz} \\ (E_t + p)v + q_y - u\tau_{yx} - v\tau_{yy} - w\tau_{yz} \end{Bmatrix} \tag{5}$$

$$G = \begin{Bmatrix} \rho w \\ \rho wu - \tau_{zx} \\ \rho vw - \tau_{zy} \\ \rho w^2 + p - \tau_{zz} \\ (E_t + p)w + q_z - u\tau_{zx} - v\tau_{zy} - w\tau_{zz} \end{Bmatrix} \tag{6}$$

The viscous stress terms are given by:

$$\tau_{xx} = \lambda(\vec{\nabla} \cdot \vec{V}) + 2\mu \frac{\partial u}{\partial x} \qquad \tau_{yy} = \lambda(\vec{\nabla} \cdot \vec{V}) + 2\mu \frac{\partial v}{\partial y} \qquad \tau_{zz} = \lambda(\vec{\nabla} \cdot \vec{V}) + 2\mu \frac{\partial w}{\partial z}$$

$$\tau_{xy} = \tau_{yx} = \mu\left(\frac{\partial u}{\partial y} + \frac{\partial v}{\partial x}\right) \qquad \tau_{xz} = \tau_{zx} = \mu\left(\frac{\partial u}{\partial z} + \frac{\partial w}{\partial x}\right) \qquad \tau_{yz} = \tau_{zy} = \mu\left(\frac{\partial w}{\partial y} + \frac{\partial v}{\partial z}\right) \tag{7}$$

The conductive heat flux terms are given by:

$$q_x = -k\frac{\partial T}{\partial x} \qquad q_y = -k\frac{\partial T}{\partial y} \qquad q_z = -k\frac{\partial T}{\partial z} \tag{8}$$

Considering a Newtonian fluid:

$$\lambda = -\frac{2}{3}\mu \tag{9}$$

The total energy is given by:

$$E_t = \rho\left(e + \frac{V^2}{2}\right) \tag{10}$$

The velocity vector, its magnitude, and its divergence are given by:

$$\vec{V} = u\,\vec{\imath} + v\,\vec{\jmath} + w\,\vec{k} \qquad V = \sqrt{u^2 + v^2 + w^2} \qquad \vec{\nabla} \cdot \vec{V} = \frac{\partial u}{\partial x} + \frac{\partial v}{\partial y} + \frac{\partial w}{\partial z} \tag{11}$$

For a calorically perfect gas, the equation of state, specific internal energy, specific heat at constant volume, and specific heat at constant pressure are given, respectively, by:

$$p = \rho RT \qquad e = c_v T \qquad c_v = \frac{R}{\gamma - 1} \qquad c_p = \gamma\, c_v \tag{12}$$

The viscosity and thermal conductivity are given by Sutherland's law and the Prandtl number relation:

$$\mu = 1{,}7894x10^{-5}\left(\frac{T}{288{,}16}\right)^{3/2}\frac{398{,}16}{T+110} \qquad k = \frac{\mu\, c_p}{\mathrm{Pr}} \tag{13}$$

B. Considerations on Computational Fluid Dynamics (CFD)

Computational Fluid Dynamics (CFD) consists of the numerical solution of the equations governing fluid flow, particularly the Navier–Stokes equations, which express the conservation of mass and momentum.

In aerodynamic applications involving large-scale vehicles such as airships, the flow exhibits predominantly turbulent characteristics, even at relatively low velocities, due to the large dimensions involved and the high Reynolds numbers. Under these conditions, CFD becomes a fundamental tool to:

- Visualize the flow behavior along the surface;
- Identify regions of acceleration, deceleration, and flow separation;
- Evaluate the formation and development of the wake;
- Estimate global aerodynamic forces, such as drag.

The use of CFD in this context allows for obtaining detailed flow information that would be difficult to access through analytical or experimental methods at this stage of the project.

Neglecting nuclear reactions and relativistic effects, mass cannot be created or destroyed. Thus, molecules, particles, fluid elements, water, among others, can be tracked within a flow field, as they do not disappear and new elements do not spontaneously appear [9]. The law of conservation of mass (Eq. 14) in a flow is based on the principle that the amount of mass entering and leaving a control volume is the same (for constant properties) [10]:

$$\frac{\partial \rho}{\partial t} + \frac{\partial(\rho u_i)}{\partial x_i} = 0 \tag{14}$$

From Newton's second law of motion (Eq. 15), the rate of change of linear momentum [11] is equal to the sum of the acting forces [10]. The first term represents the rate of increase of momentum per unit volume in the control volume. The second term represents the rate of momentum loss per unit volume through the control surface. The next two terms represent surface forces due to external stresses per unit volume, namely pressure and shear stress. The penultimate term represents body forces due to gravity and thermal expansion of the fluid. The last term refers to a source term [12]:

$$\frac{\partial(\rho U_i)}{\partial t} + \rho\frac{\partial(\rho U_i)}{\partial x_j} = \frac{\partial p}{\partial x_i} + \frac{\partial p}{\partial x_j}\left[\mu\left(\frac{\partial U_i}{\partial U_j} + \frac{\partial U_j}{\partial U_i} - \frac{2}{3}\frac{\partial U_k}{\partial U_k}\partial_{ij}\right)\right] + \rho g_i + F \tag{15}$$

The energy equation (Eq. 16) is derived from the first law of thermodynamics, which states that the rate of change of energy of a fluid particle is equal to the rate of heat addition plus the rate of work done on the particle [13]:

$$\frac{\partial(\rho E)}{\partial t} + \frac{\partial[U_i(\rho E+p)]}{\partial x_i} = \frac{\partial}{\partial x_i}\left[k_{ef}\frac{\partial T}{\partial x_i} - \sum_j h_j J_{j,i}\left(\tau_{ij}\right)_{ef}\right] + S_{ij} \tag{16}$$

where ρ is the fluid density; U_i, U_j, U_k are velocity components; x_i, x_j are spatial coordinates; T is temperature; g is gravitational acceleration; F is an external body force or user-defined source term; μ is viscosity; p is pressure; τ is the stress tensor; t is time; E is specific enthalpy; J is the diffusive flux component; k_{ef} is thermal conductivity; h is specific heat; and S_{ij} is a source term.

For the numerical computational analysis, the commercial software ANSYS Fluent will be used, which applies the finite volume method based on the fundamental principles described above.

Considering numerical analysis, another important parameter is the hydraulic diameter, which can be calculated as:

$$D_h = \frac{4A}{P_w} \tag{17}$$

where A is the area and P_w is the wetted perimeter.

IV. Analytical Boundary-Layer Analysis

The analytical modeling was performed to characterize the evolution of the laminar and turbulent boundary layers along the airship hull, assumed to approximate a prolate spheroid at low angle of attack.

A. Laminar Regime (Blasius Approximation)

For the initial region (x/L < 0.1), the laminar boundary layer thickness δ, displacement thickness δ*, and momentum thickness θ are given by:

$$\delta(x) = 5.0\sqrt{\frac{\nu x}{U_\infty}}, \delta^*(x) = 1.72\sqrt{\frac{\nu x}{U_\infty}}, \theta(x) = 0.664\sqrt{\frac{\nu x}{U_\infty}} \tag{18}$$

The local skin friction coefficient is:

$$C_{f,lam} = \frac{0.664}{\sqrt{Re_x}} \tag{19}$$

as derived by Blasius and extensively validated for laminar flat-plate flows [5].

B. Turbulent Regime (Prandtl–Schlichting Approximation)

For 0.1 < x/L < 1:

$$\delta(x) = 0.382xRe_x^{-1/5}, C_{f,turb} = 0.0592Re_x^{-1/5} \tag{20}$$

Integrating across the hull yields a mean skin friction coefficient $C_{f,mean} \approx 0.0024$ [14].

C. Transition and Separation

The critical Reynolds number for transition ($Re_{x,cr} \approx 3 \times 10^5$) occurs near x/L ≈ 0.02, confirming that the boundary layer becomes fully turbulent almost immediately [10]. Analytical pressure gradients were incorporated using the momentum integral equation.:

$$\frac{d\theta}{dx} + (2+H)\frac{\theta}{U_e}\frac{dU_e}{dx} = \frac{C_f}{2} \quad (21)$$

where $H = \delta^*/\theta \approx 1.4–1.6$ for turbulent flow. The integration indicates mild adverse gradients near the tail, predicting possible flow detachment beyond $x/L \approx 0.95$ [15].

V. Description of the Geometric Model

The geometric model analyzed (Figure 2) corresponds to the Explorer airship, whose main dimensions are:

- Total length: **100 m**
- Maximum diameter: **16.9 m**
- Maximum frontal area (reference area): **224.3 m²**

The geometry considered includes the main body of the airship, tail, and gondola. Internal elements and construction details that do not directly influence the external flow were neglected, allowing the analysis to focus on the aerodynamics of the envelope.

In order to reduce computational cost, a longitudinal symmetry plane was adopted, considering only half of the geometry during the simulation. This approach is valid for flows aligned with the longitudinal axis, with no angle of attack or crosswind. The aerodynamic forces obtained were subsequently adjusted to represent the complete vehicle, ensuring that the final results correspond to the full airship.

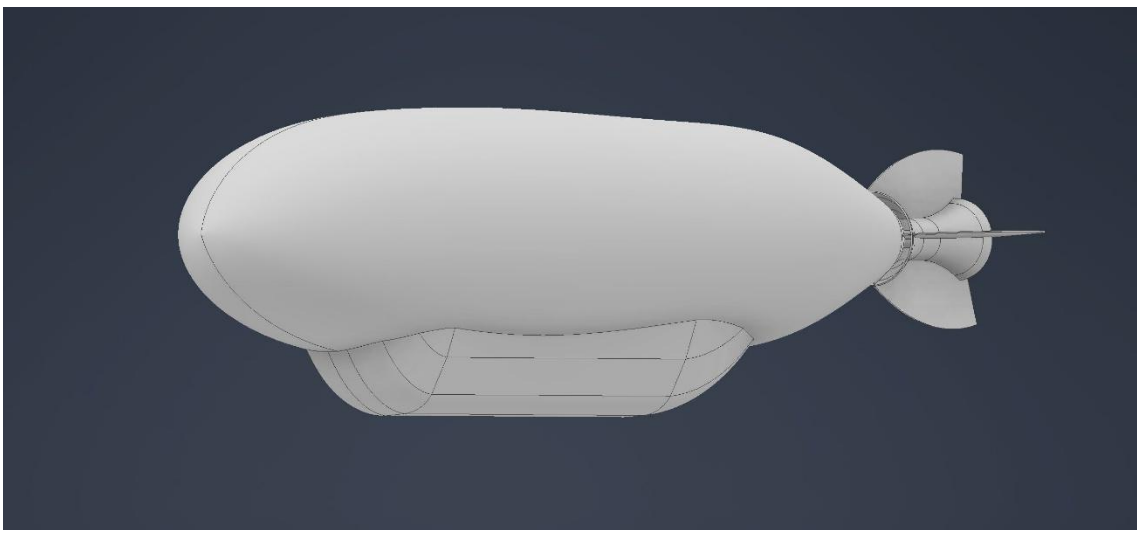

Figure 2 – 3D Geometric Model of the EXPLORER Airship.

VI. Numerical Methodology (ANSYS Fluent 2025 R2)

A. Computational Setup

The simulations were carried out using ANSYS Fluent 2025R2, considering the following assumptions:

- Three-dimensional (3D) simulation;
- Steady-state regime;
- Atmospheric conditions at sea level;
- Zero angle of attack.

The inlet velocity was set to **58 m/s and 39 m/s**, with an air density of **1.225 kg/m³**.

A 3D axisymmetric transient simulation was carried out using the ANSYS Fluent 2025 R2 solver [3,9]. The main solver configuration is summarized below:

Setting	Option
Solver type	Pressure-based, transient
Coupling scheme	Coupled
Discretization	2nd-order upwind (momentum, turbulence, energy)
Temporal scheme	2nd-order implicit
Turbulence model	k–ω SST (with near-wall correlation)
Compressibility	Ideal gas model, low-Mach correction
Time step	1×10^{-3} s, 10,000 iterations
Domain	Axisymmetric
Inlet velocity	58 m/s / 39 m/s
Turbulence intensity	5%
Turbulent viscosity ratio	10
Outlet	Pressure outlet (101325 Pa)
Wall condition	No-slip, adiabatic

B. Turbulence Model

The turbulence model adopted was the k–ω SST (Shear Stress Transport) model, widely used in external aerodynamic analyses.

This model combines the accuracy of the k–ω model in the near-wall region with the robustness of the k–ε model in regions away from the surface. Its main advantages include:

- Good representation of the boundary layer;
- Ability to predict flow separation;
- Robustness in flows with adverse pressure gradients.

Considering the elongated geometry of the airship and the importance of pressure recovery in the aft region, the k–ω SST model is well suited for the proposed analysis.

C. Computational Domain

The computational mesh was generated using unstructured tetrahedral elements, totaling approximately:

- 2.3 million nodes
- 6.5 million elements

Mesh refinements were applied along the airship surface (inflation), enabling proper resolution of the boundary layer and viscous effects. The mesh refinement was concentrated in the following regions:

- Airship nose (stagnation region);
- External surface of the body;
- Aft region and rear appendages;
- Downstream wake region.

The transition between refined regions and the free-stream flow was performed gradually, ensuring numerical stability and an accurate representation of pressure and velocity gradients.

The numerical model considered a rectangular computational domain with approximate dimensions of 1000 m × 1500 m × 1500 m, as shown in Figure 3.

Figure 4 illustrates the mesh refinement at the core of the Explorer airship geometry, providing a closer view of the region of interest.

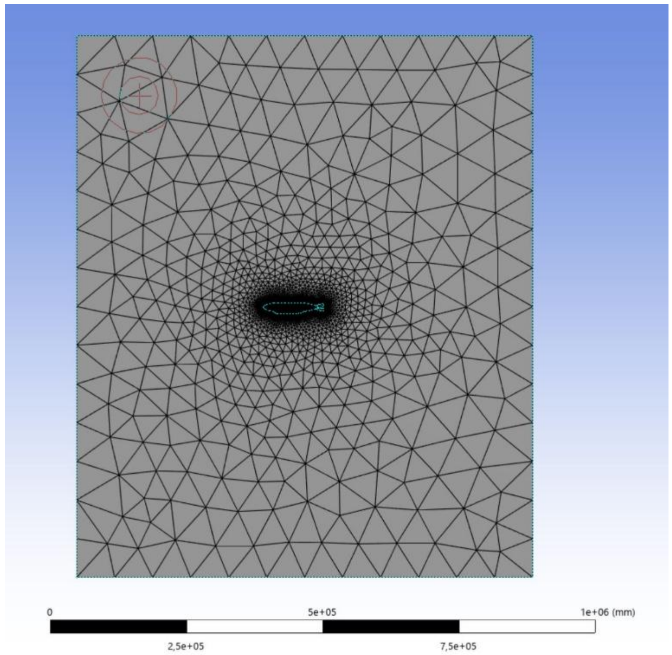

Figure 3 – 3D Complete Computational Domain of the Explorer Airship.

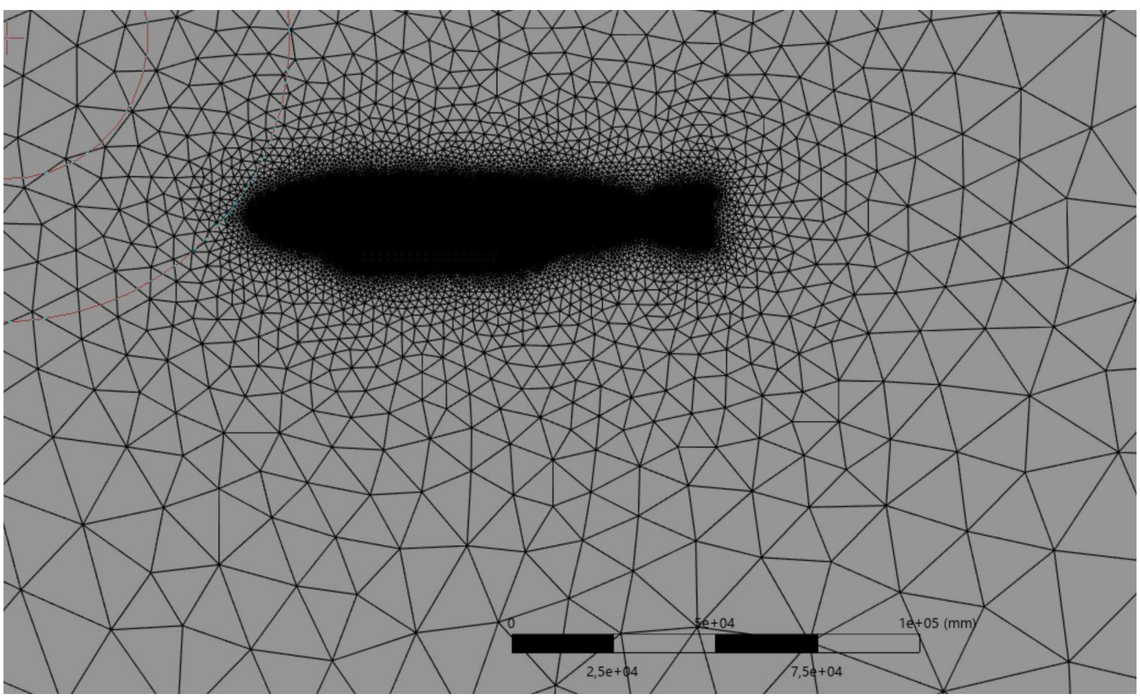

Figure 4 – Mesh Close-Up View Along the Computational Domain of the Explorer Airship.

D. Mesh and Near-Wall Resolution

The mesh consisted of ~7.7×10^5 quadrilateral elements, generated using the Quad Dominant and Sweep methods [4]. Refinement layers were applied along the hull with a growth rate ≤ 1.2 and first cell height ensuring $y^+ < 1$.

Parameter	**Value**
Nodes	772,290
Elements	767,171
y^+ (average)	0.7
Growth rate	1.18
Farfield extent	20D upstream, 30D downstream

This ensured accurate capture of viscous sublayer gradients and boundary-layer evolution without wall functions [4].

Figure 5 highlights the structured and refined mesh in the tail ejector region of the Explorer airship, which is one of the key areas of interest in this analysis.

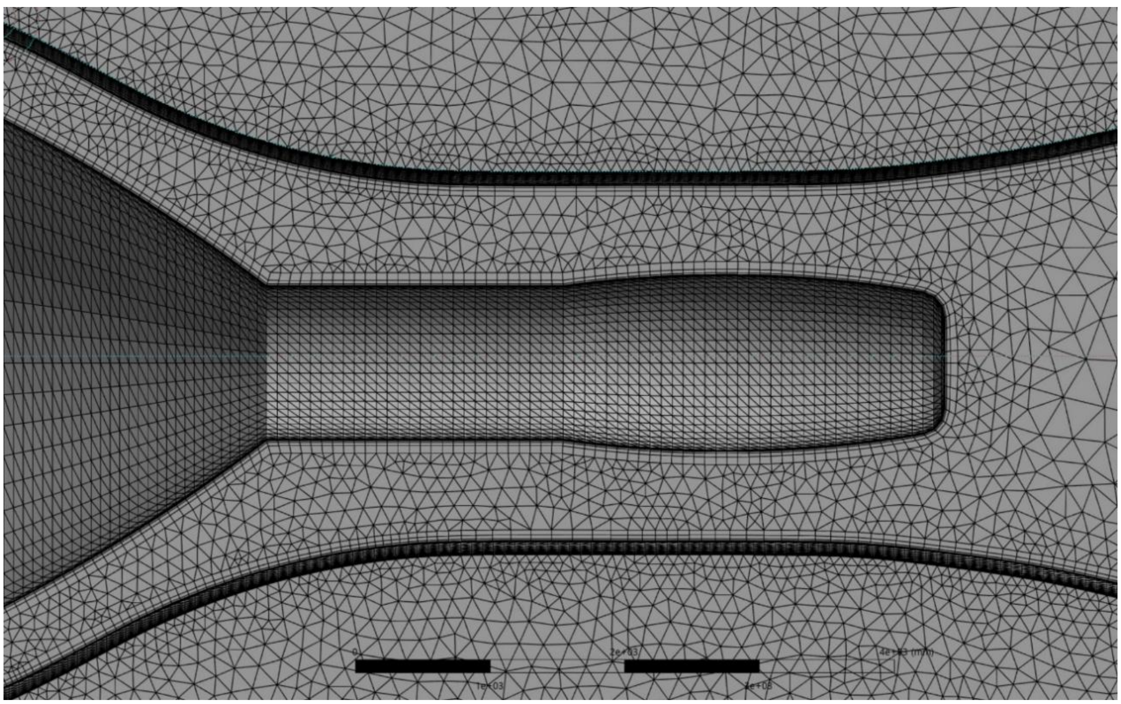

Figure 5 – 3D Mesh Refinement Detail in the Tail Ejector Region of the Explorer Airship.

VII. Results and Discussion

A. Pressure Distribution for 58 m/s

The wall pressure distribution (Figure 6) shows a stagnation peak of approximately 1.03×10^5 Pa, followed by a gradual decrease to 1.00×10^5 Pa along the body midsection [15]. At $x/L \approx 0.95$–1.0, oscillations occur due to mild separation, with the static pressure recovering partially downstream.

When normalized by the dynamic pressure ($q = \frac{1}{2}\rho V^2 \approx 2{,}056$ Pa), the minimum $C_p \approx -0.25$, which is typical for streamlined, slender bodies [14].

Along the main body, a smooth pressure distribution is observed, indicating that the flow remains predominantly attached to the surface (Figure 7).

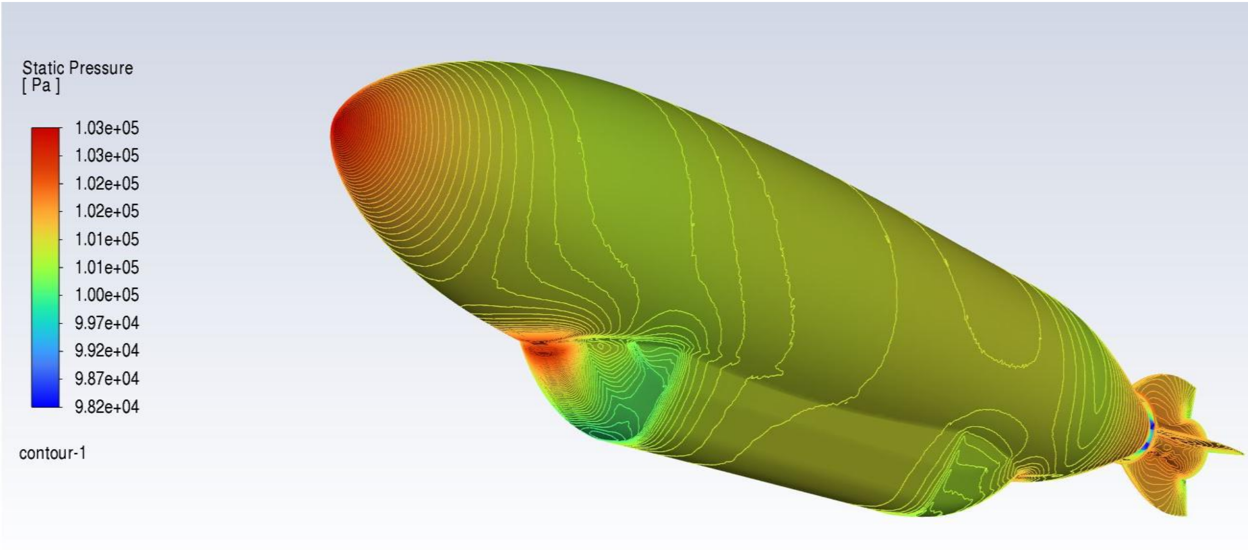

Figure 6 – 3D View of the Pressure Contour Along the Explorer Airship for 58 m/s.

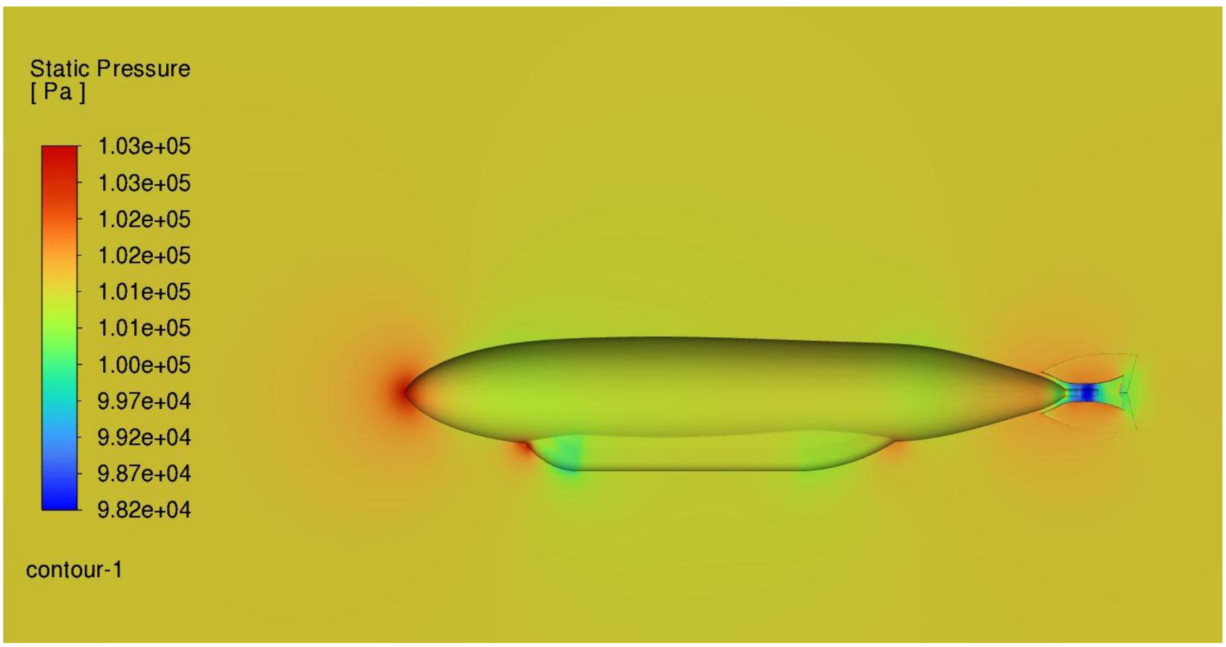

Figure 7 – Pressure Contour Along the Explorer Airship for 58 m/s.

In the tail region (Figure 8), a pressure drop occurs associated with the partial recovery of the flow. This region is identified as the main contributor to the vehicle's pressure drag. It can be observed that the pressure reaches a value of approximately 9.82×10^4 Pa.

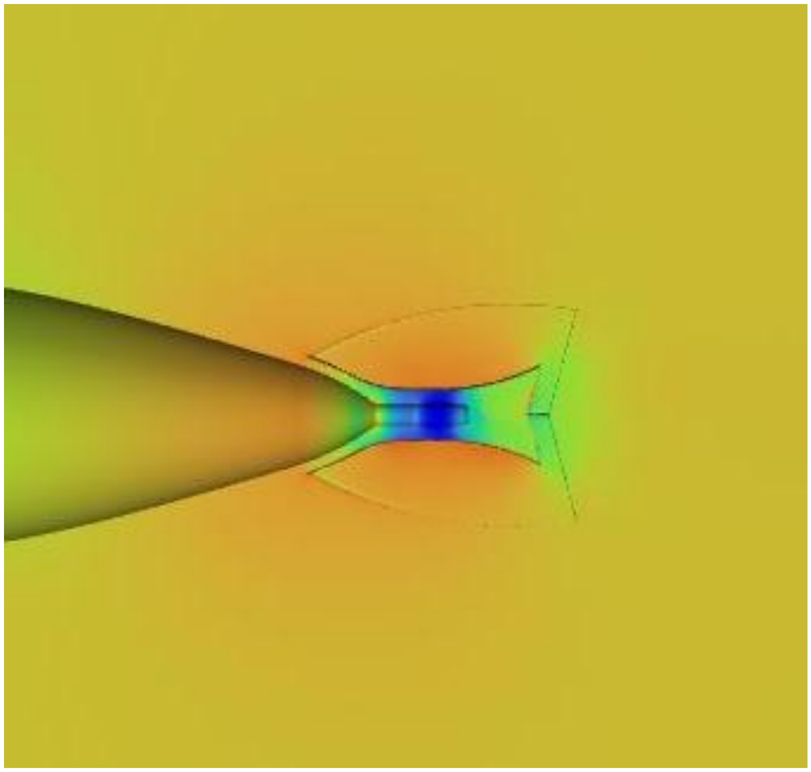

Figure 8 – Pressure Contour Highlighting the Tail Region of the Explorer Airship for 58 m/s.

B. Flow Field Velocity

The velocity contour reveals a smooth external flow pattern with no major separation up to x/L ≈ 0.9 [15]. A small recirculation bubble forms near the tail, consistent with predictions from the analytical model [14].

The freestream velocity reaches 58 m/s in localized regions near the upper curvature due to streamline contraction, while the near-wall velocity decreases smoothly, indicating stable pressure recovery [2].

The velocity fields indicate a controlled acceleration of the flow around the nose, followed by attached flow along the main body. The wake formed downstream shows moderate thickness and a gradual recovery of velocity, with no evidence of significant flow separation or pronounced instabilities.

This behavior is characteristic of streamlined, elongated bodies and indicates acceptable levels of viscous drag for the analyzed geometry. The maximum velocity observed in the model was 86 m/s, as shown in Figures 9 and 10 (tail ejector).

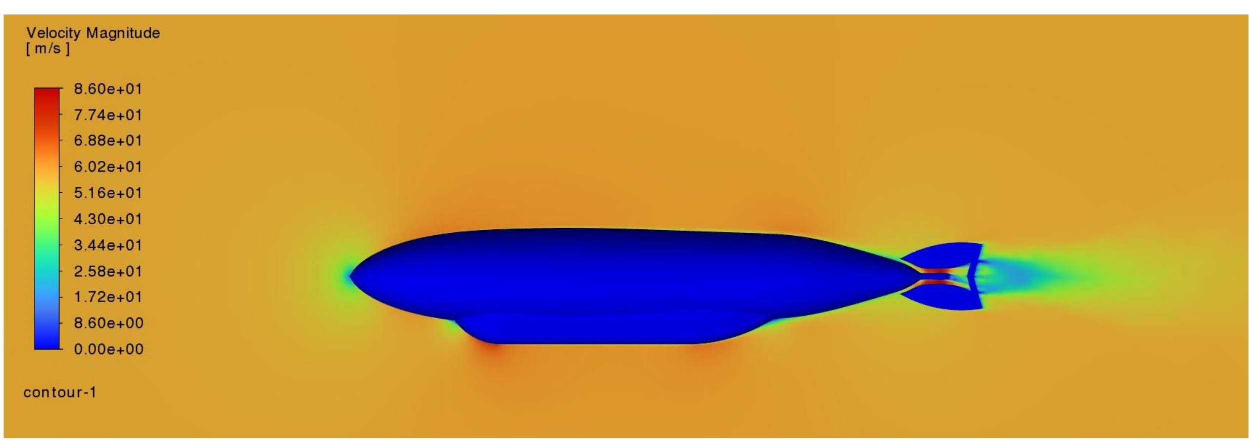

Figure 9 – Pressure Contour Highlighting the Tail Region of the Explorer Airship for 58 m/s.

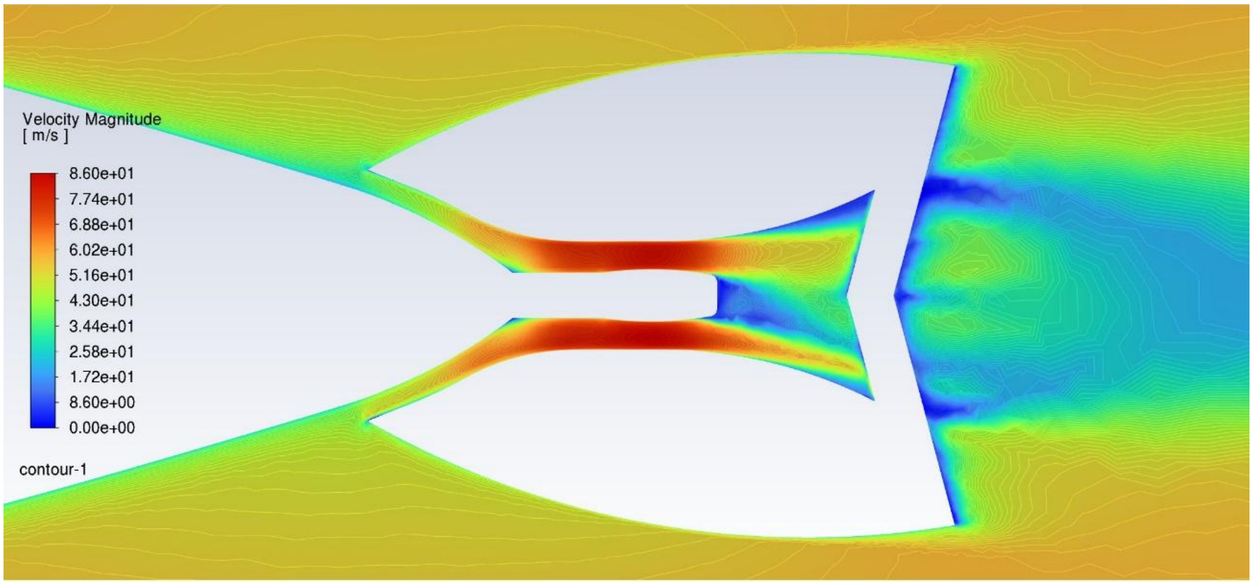

Figure 10 – Velocity Contour Highlighting the Tail Region of the Explorer Airship for 58 m/s.

It is worth noting that near the passenger gondola, a small boundary layer separation was observed, which quickly reattached to the surface. This behavior is observed in the frontal region of the gondola (Figure 11) and in the rear region of the gondola (Figure 12).

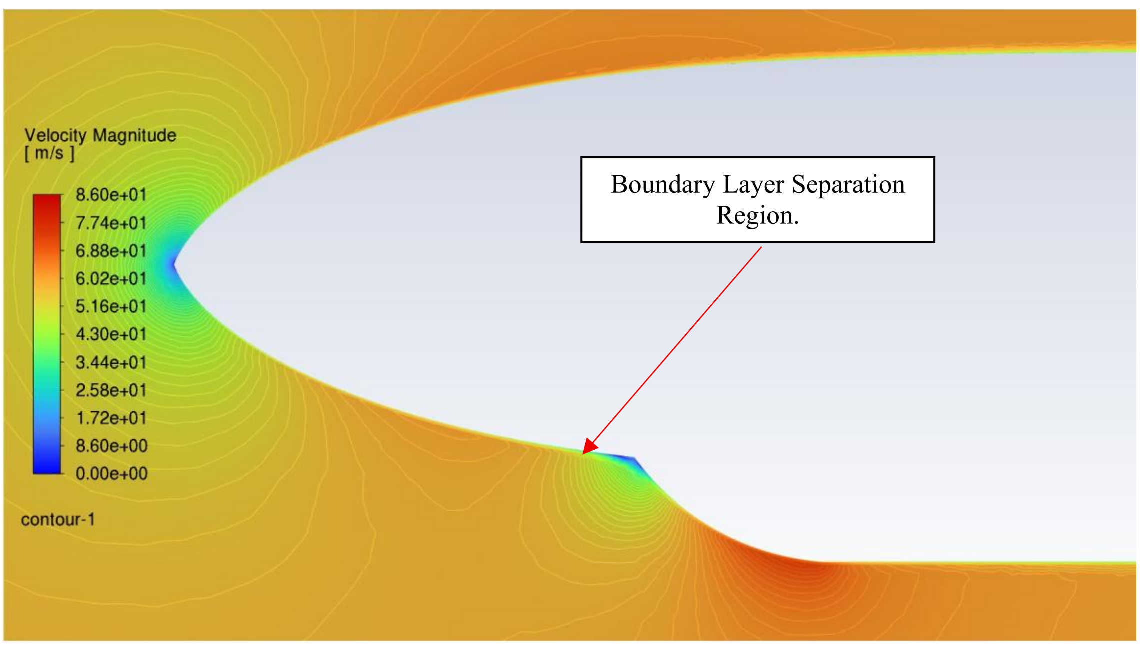

Figure 11 – Velocity Contour Highlighting the Boundary Layer Separation Region at the Front Section of the Explorer Airship Gondola for 58 m/s.

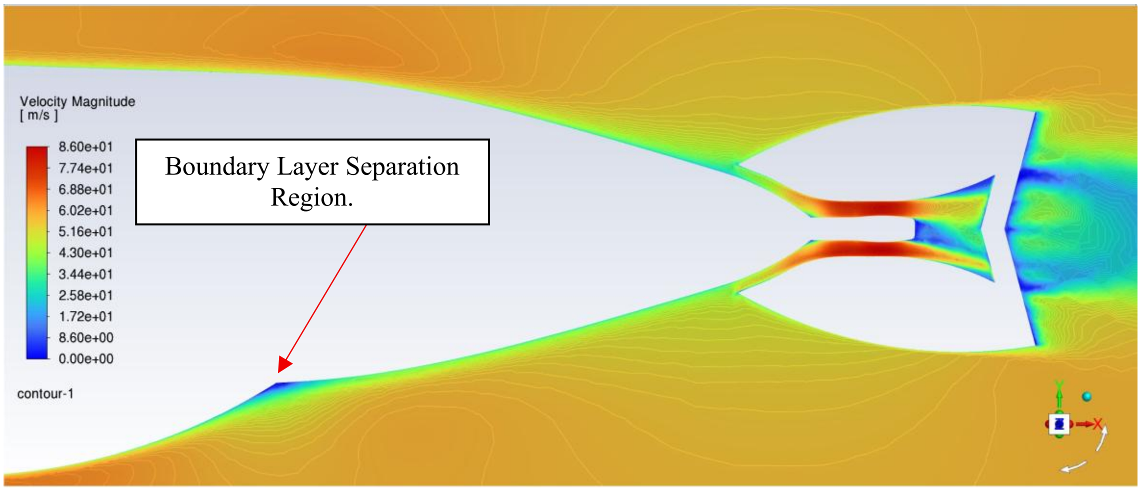

Figure 12 – Velocity Contour Highlighting the Boundary Layer Separation Region at the Rear Section of the Explorer Airship Gondola for 58 m/s.

C. Pressure Distribution for 39 m/s

The static pressure contours (Figure 13) show a well-defined stagnation point in the frontal region of the airship, characterized by high pressure values on the order of **1.02 × 10⁵ Pa**, as shown in Figures 13–16. Along the main body, a smooth pressure distribution is observed, indicating that the flow remains predominantly attached to the surface.

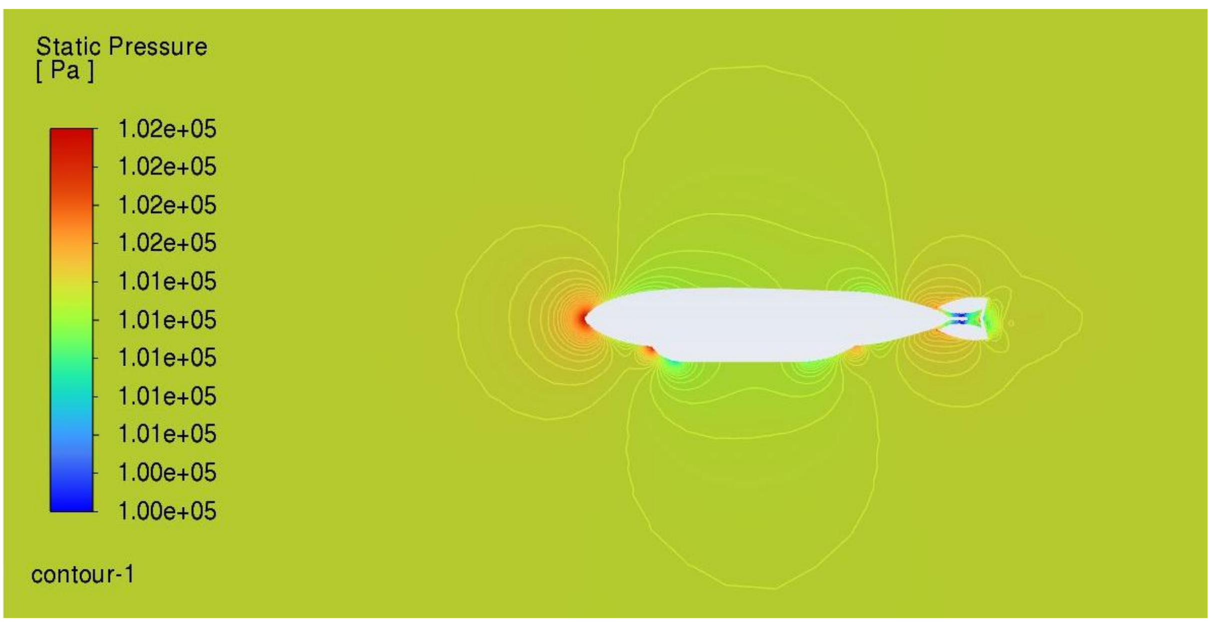

Figure 13 – Side View of Static Pressure Contour Along the Explorer Airship at 39 m/s.

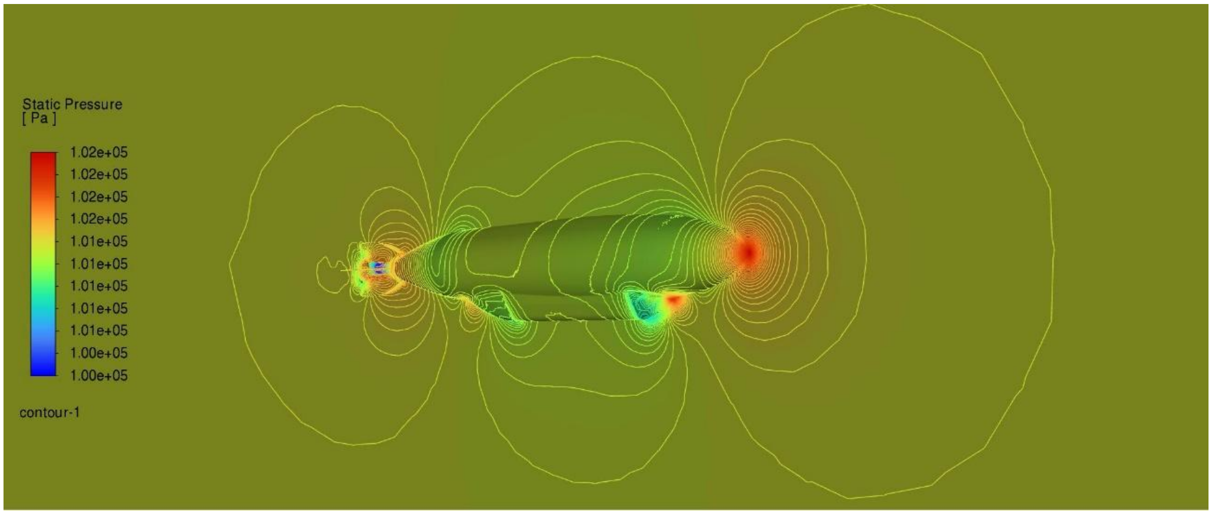

Figure 14 – 3D Static Pressure Contour Along the Explorer Airship at 39 m/s.

In the tail region (Figures 13 and 16), a pressure drop occurs associated with the partial recovery of the flow. This region is identified as the main contributor to the vehicle's pressure drag. It can be observed that the pressure reaches a value of approximately **1.002×10^5 Pa**.

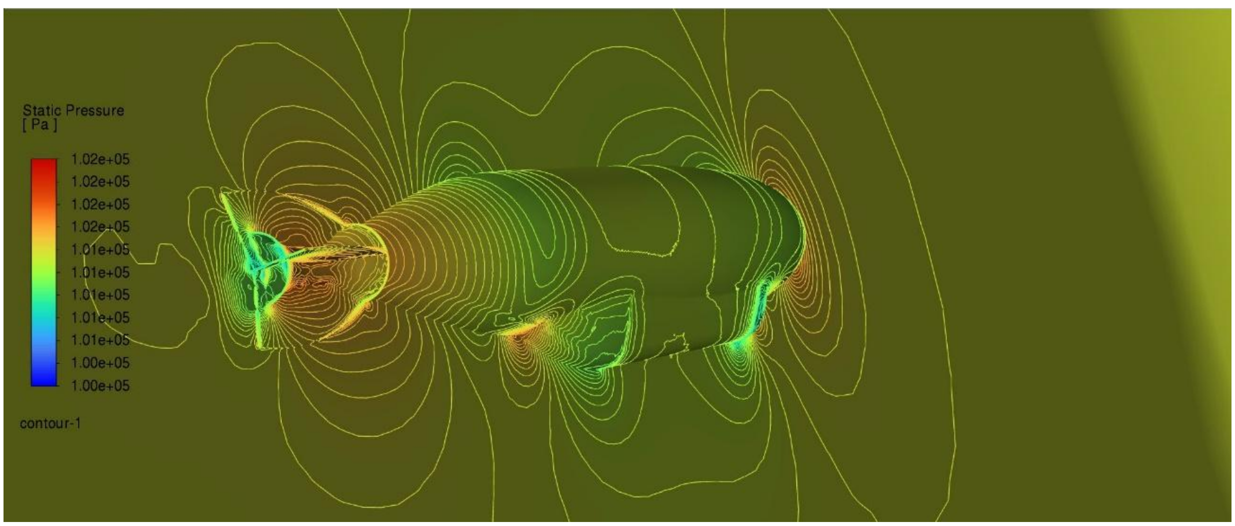

Figure 15 – Rear View of the Static Pressure Contour Along the Explorer Airship at 39 m/s.

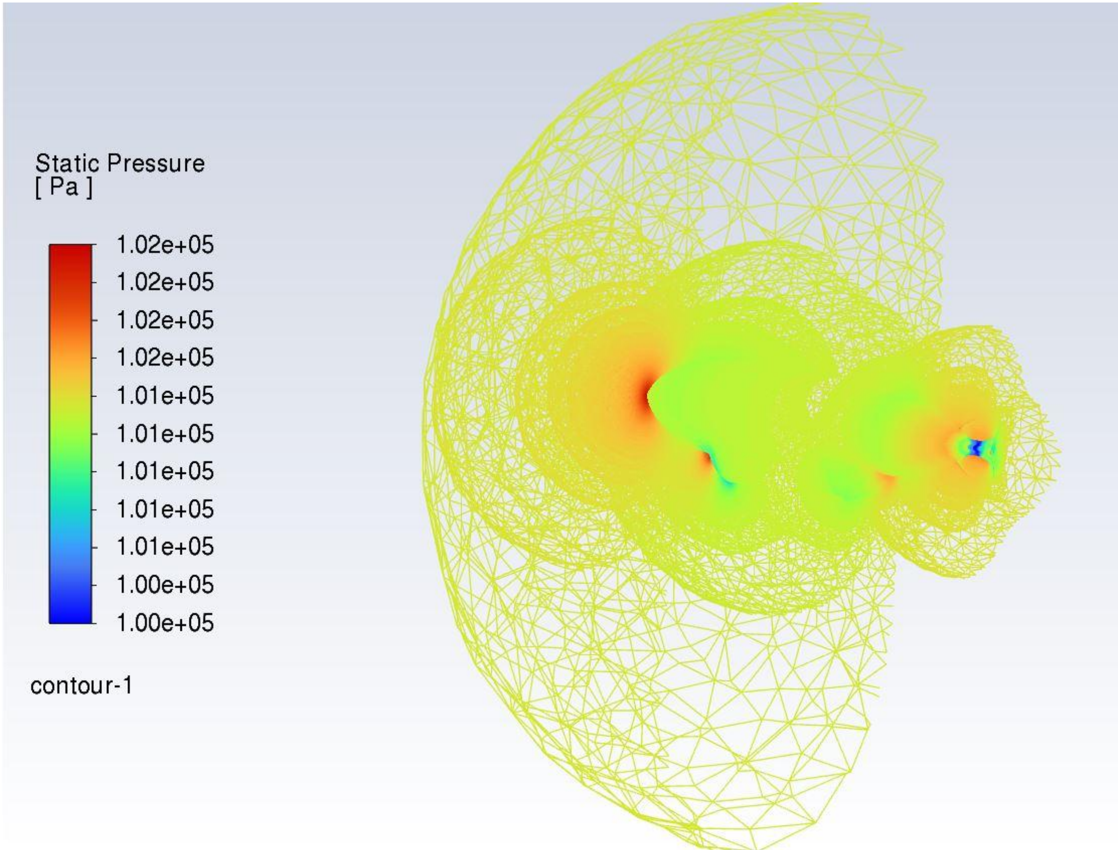

Figure 16 – 3D Static Pressure Contour Along the Explorer Airship at 39 m/s, Showing the Pressure Propagation Generated by the Vehicle.

D. Total Pressure Distribution for 39 m/s

The total pressure distribution (Figure 17) along the flow is an important indicator of energy losses associated with viscous and dissipative effects, allowing an assessment of the vehicle's aerodynamic efficiency.

From the obtained results, the following characteristics can be observed:

- Conservation of total pressure in regions of predominantly inviscid flow, where dissipative effects are negligible;
- Significant reduction of total pressure in the wake region, indicating energy losses associated with turbulent dissipation and flow mixing;
- Formation of a low energy-recovery zone downstream of the vehicle, characterized by a persistent total pressure deficit.

These effects are directly related to aerodynamic drag, since the reduction in total pressure represents the irreversible conversion of the flow's mechanical energy into internal (dissipated) energy. Therefore, the magnitude and extent of the total pressure deficit region are key indicators of the overall aerodynamic performance of the system.

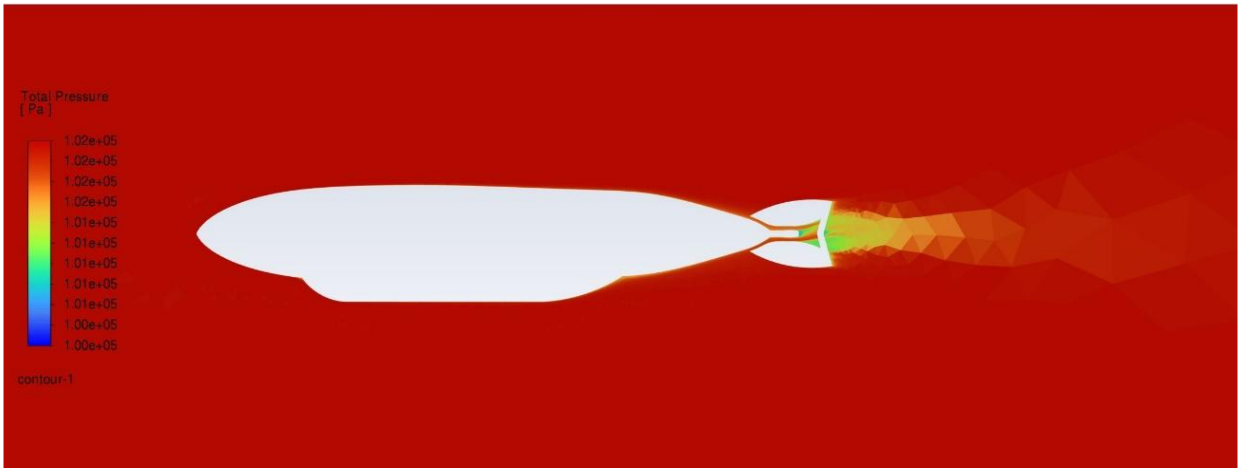

Figure 17 – Total Pressure Contour Along the Explorer Airship at 39 m/s, Indicating Losses Associated with Turbulent Dissipation.

E. Absolute Pressure Distribution for 39 m/s

The analysis of absolute pressure in the computational domain allows verification of the physical consistency of the numerical solution, in addition to complementing the interpretation of the static and total pressure fields.

The results (Figure 18) indicate behavior consistent with low-speed subsonic flows, characterized by a Mach number on the order of $M \approx 0.11$. Under these conditions, the following characteristics are observed:

- Small pressure variations relative to the absolute level, indicating low flow compressibility;
- Approximately incompressible regime, in which density variations are negligible for engineering analysis;
- Predominance of static pressure over dynamic pressure, with the latter accounting for only a fraction of the total flow pressure.

This behavior is consistent with subsonic flow theory at low Mach numbers, reinforcing the adequacy of the assumptions adopted in the numerical modeling and the reliability of the obtained results.

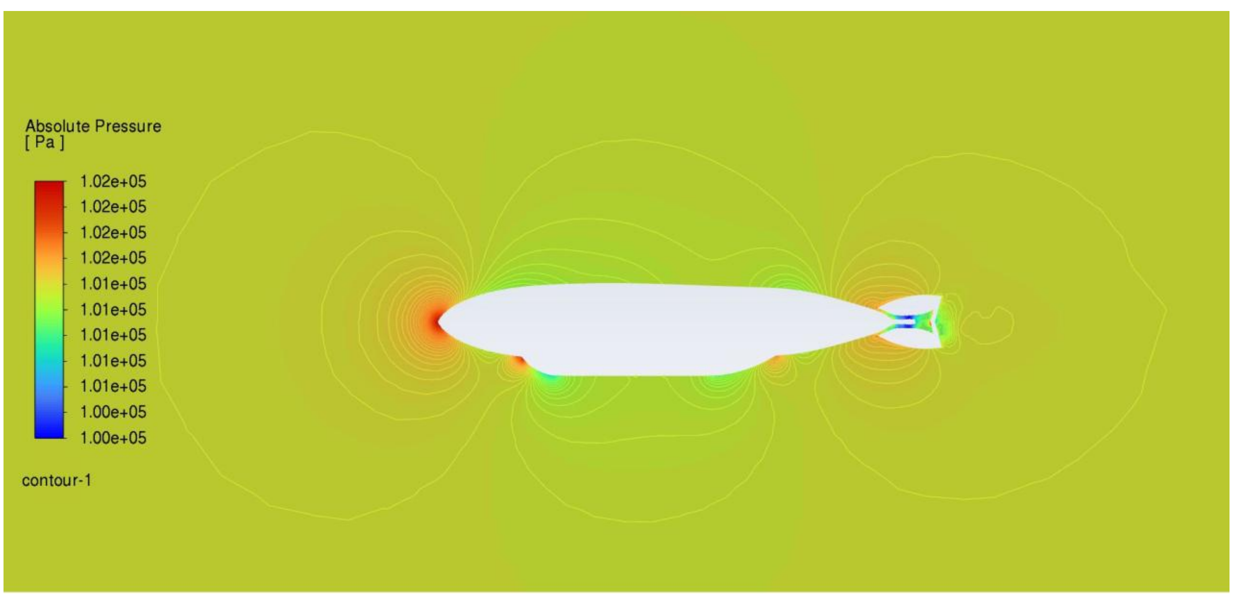

Figure 18 – Absolute Pressure Contour Along the Explorer Airship at 39 m/s.

F. Static and Total Temperature Fields

The distributions of static temperature (Figure 19) and total temperature (Figure 20) throughout the computational domain show minimal variation, indicating a low influence of thermal effects on the analyzed flow.

From the results, the following aspects can be highlighted:

- Nearly uniform temperature, with values close to 300 K across the entire domain;
- Small localized variations, mainly in the wake region, associated with viscous dissipation and the conversion of mechanical energy into internal energy;
- Absence of significant thermal gradients, indicating that thermal effects do not have a meaningful impact on the aerodynamic behavior of the flow.

This behavior is consistent with a low-speed subsonic flow regime, in which compressibility and aerodynamic heating effects are negligible. Therefore, the analysis can be conducted with a primary focus on aerodynamic phenomena, without the need for coupling with more complex thermal models.

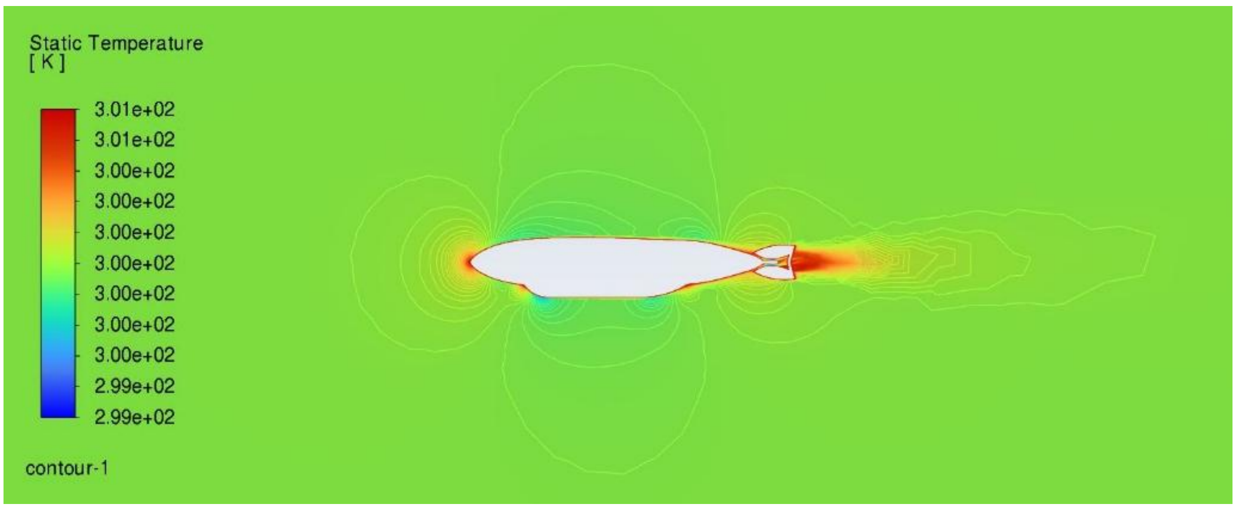

Figure 19 – Static Temperature Contour Along the Explorer Airship at 39 m/s.

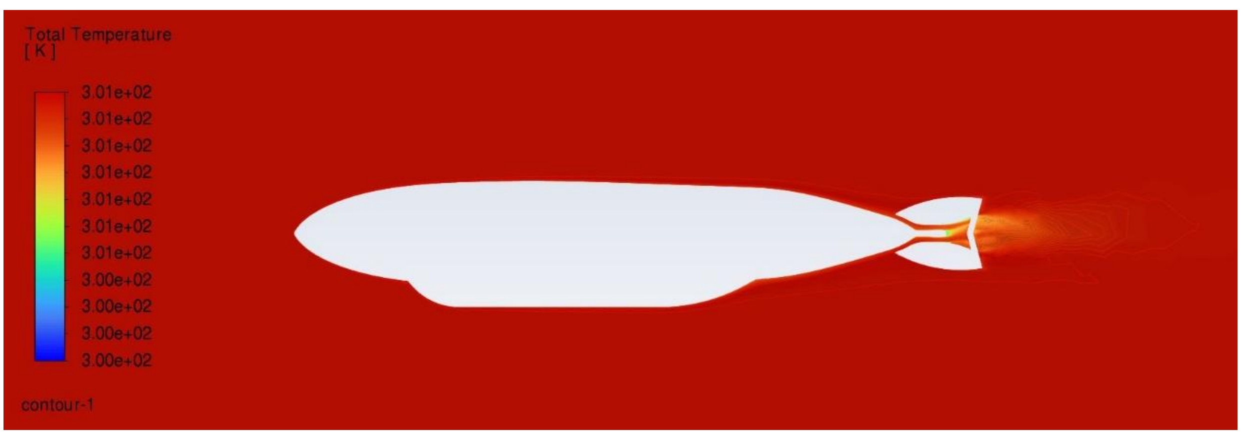

Figure 20 – Total Temperature Contour Along the Explorer Airship at 39 m/s.

G. Flow Field Velocity

No abrupt boundary layer separations were identified along the main body, indicating a geometry with good aerodynamic continuity and predominantly attached flow in this region.

However, it is observed that the transition region between the main body and the empennage exhibits localized flow acceleration, accompanied by signs of partial boundary layer separation. This behavior contributes to an increase in aerodynamic drag, making it a critical area for future analysis and potential geometric optimization.

The maximum velocity indicated in the model was 54 m/s, as shown in Figures 21 and 22.

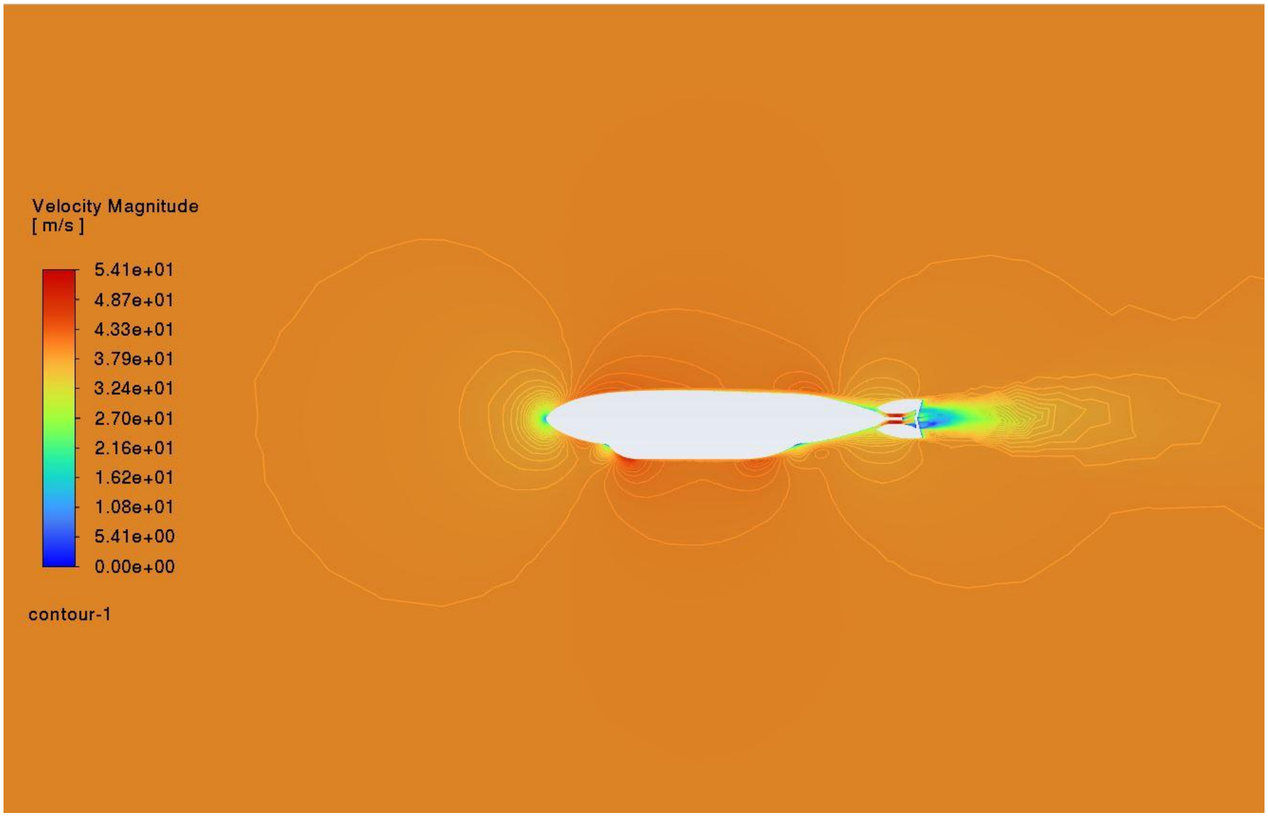

Figure 21 – Velocity Contour Along the Explorer Airship at 39 m/s.

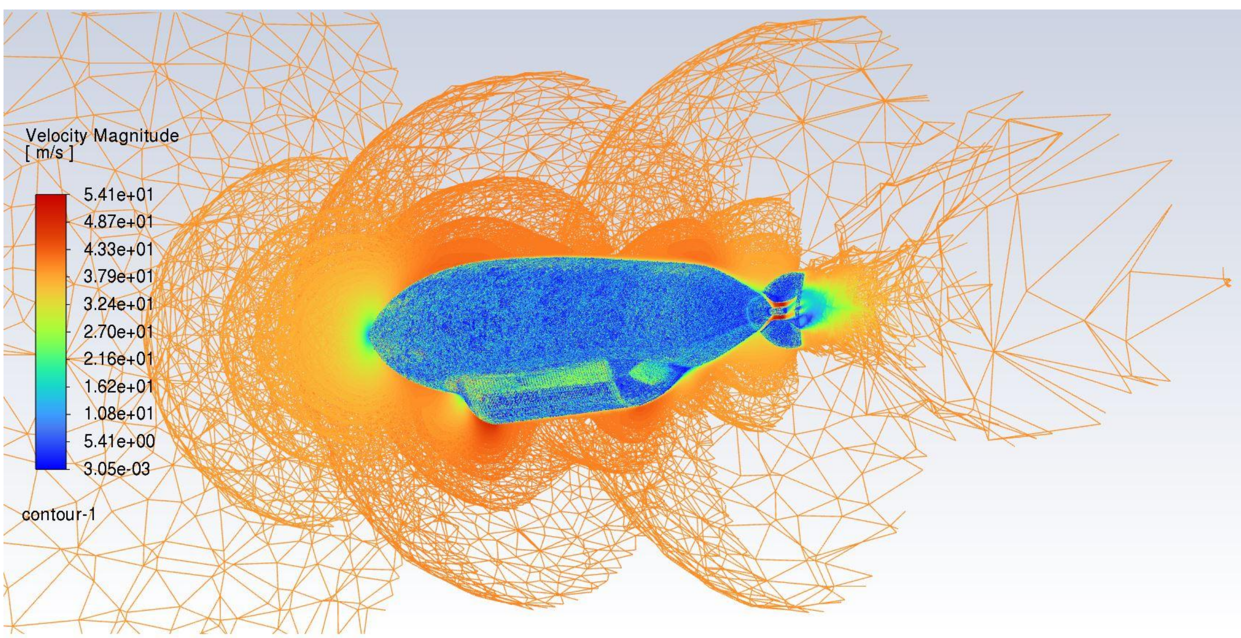

Figure 22 – 3D View of the Velocity Contour Highlighting the Tail Region of the Explorer Airship at 39 m/s.

H. Mach Number

The analysis of the Mach number field (Figures 23) within the computational domain allows characterization of the flow regime and evaluation of the relevance of compressibility effects.

The obtained results indicate:

- Maximum Mach number values on the order of 0.15, observed in localized regions of flow acceleration;
- Fully subsonic regime, with no occurrence of phenomena associated with transonic or supersonic flows;
- Absence of significant compressibility effects, since fluid density variations remain negligible throughout the domain.

Therefore, the incompressible flow assumption adopted in the numerical modeling is appropriate for the analyzed conditions, with no relevant influence of compressibility effects on the obtained results.

This result reinforces the physical consistency of the simulation and validates the use of simplified models for aerodynamic analysis within the considered operating regime.

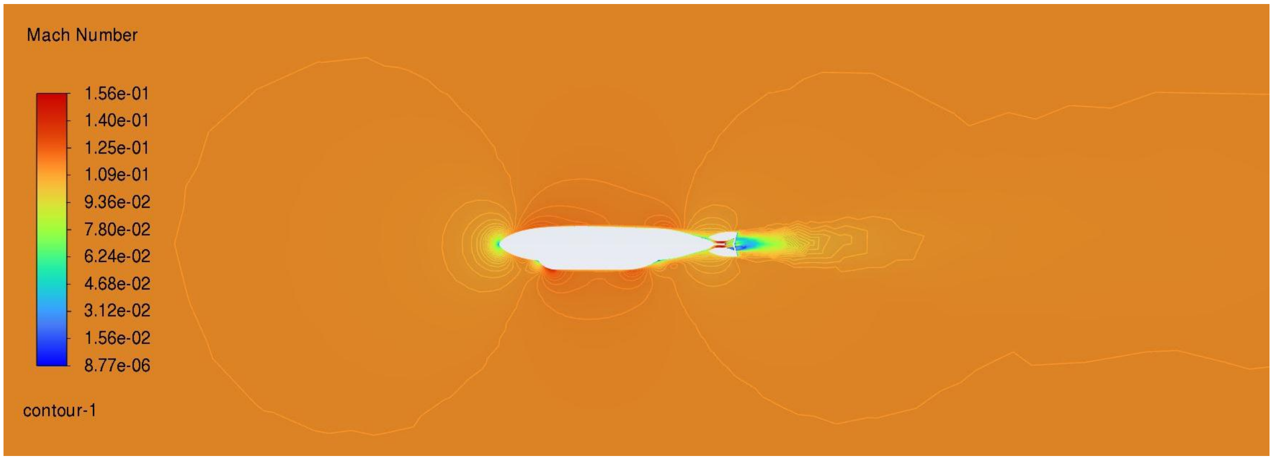

Figure 23 – Mach Number Contour Along the Explorer Airship at 39 m/s.

I. Drag Force and Drag Coefficient

The total aerodynamic drag force, adjusted to represent the complete vehicle, was:

D = 40,408 N (58 m/s) and 18,345 N (39 m/s)

The global drag coefficient was calculated using the expression:

$$C_D = \frac{D}{\frac{1}{2}\rho V^2 A} \tag{22}$$

where:

ρ = 1,225 kg/m³
V = 58 m/s and 39 m/s
A = 224,3 m²

Resulting in:

$$\boldsymbol{C_D \approx 0.21\ (58\ \mathrm{m/s})\ \text{and}\ 0.0778\ (39\ \mathrm{m/s})}$$

This value is consistent with large-scale, elongated airships, considering the presence of external appendages and the lack of specific optimizations in the aft region.

VIII. Discussions

A. Discussions for 58 m/s

The detailed analysis of the simulation results demonstrates that the flow remains predominantly attached to the airship body over nearly its entire surface, with no significant boundary layer separation observed under the analyzed conditions. This behavior indicates that the adopted geometry promotes a smooth flow transition and contributes to maintaining the overall aerodynamic stability of the configuration, reducing energy losses associated with premature flow separation.

It is also verified that the total drag is predominantly influenced by the pressure drag contribution, especially in the rear region of the envelope, where adverse pressure gradients tend to intensify wake formation. This characteristic is consistent with large-volume, elongated bodies, in which form drag plays a more significant role than skin-friction drag. The calculated drag coefficient is physically consistent with the considered geometry and the flow regime adopted in the simulations, remaining within the expected range for airships of similar scale.

Overall, the obtained results reinforce the consistency of the adopted modeling approach and confirm the suitability of the Explorer model as a preliminary aerodynamic evaluation platform within the Eternaus Project, providing reliable technical support for project refinement and subsequent development stages.

B. Comparative Analysis of Operating Conditions

In order to evaluate the physical consistency of the numerical results and the influence of flow velocity on the aerodynamic behavior of the Explorer airship, a comparative analysis was conducted between two distinct operating conditions, both at sea level.

The analyzed conditions are defined as follows:

- **Case 1:** flow velocity of 58 m/s;
- **Case 2:** flow velocity of 39 m/s.

This approach makes it possible to investigate the sensitivity of aerodynamic forces and flow fields to velocity variation, as well as to verify the consistency of the results with the fundamental laws of aerodynamics, particularly the quadratic dependence of drag on velocity in subsonic regimes.

Table 1 - Comparação entre resultados das simulações com velocidades 39 m/s e 58 m/s.

Parameter	**58 m/s**	**39 m/s**	**Expected Variation**	**Observation**
Velocity (m/s)	58	39	—	Problem input
Mach Number	~0.17	~0.11	Linear with V	Subsonic regime
Dynamic Pressure (Pa)	~2060	~930	$\propto V^2$	Increase of ~2.2×
Total Drag (N)	~40,408	~18,345	$\propto V^2$	Consistent
Pressure Drag (N)	↑	~10,473	$\propto V^2$	Dominant
Viscous Drag (N)	↑	~7,871	$\propto V^2$ (approx.)	Boundary layer influence
Wake Structure	More intense	Moderate	↑ with V	Greater dissipation
Pressure Gradients	Higher	Moderate	↑ with V^2	Higher aerodynamic loading
Compressibility	Negligible	Negligible	—	Mach < 0.3
Temperature	~300 K	~300 K	—	No relevant thermal effects
Required Power	2.34 MW (≈ 3,182 hp)	0.71 MW (≈ 965 hp)	$\propto V^3$	Strong dependence on velocity
Installed Power (+30%)	3.05 MW (≈ 4,136 hp)	0.92 MW (≈ 1,255 hp)	$\propto V^3$	Includes operational margin

The results presented in Table 1 demonstrate strong physical consistency with the fundamental principles of aerodynamics. In particular, it is observed that aerodynamic drag varies proportionally to the square of the velocity: $D \propto V^2$, while the required power exhibits a cubic dependence: $P \propto V^3$, as expected for subsonic flows.

Additionally, it is verified that increasing the velocity results in wake intensification, higher pressure gradients, and consequently greater energy dissipation within the flow. Despite these variations, the regime remains fully subsonic, with no significant influence from compressibility or thermal effects.

These results reinforce the reliability of the numerical modeling and provide a solid basis for the preliminary sizing of the propulsion system and future aerodynamic optimization studies.

C. Verification of the Drag Law

For incompressible flows in the subsonic regime, aerodynamic drag is proportional to the square of the flow velocity, according to the relation: $D \propto V^2$.

In order to verify the consistency of the results obtained from the numerical simulation, a comparative analysis was performed between the two velocity conditions considered.

The ratio between the velocities is given by:

$$\frac{V_2}{V_1} = \frac{58}{39} \approx 1.49$$

Squaring this ratio, according to the theoretical relationship:

$$\left(\frac{V_2}{V_1}\right)^2 \approx 2.21$$

On the other hand, the ratio between the total drag values obtained numerically is:

$$\frac{D_2}{D_1} = \frac{40{,}408}{18{,}345} \approx 2.20$$

An excellent agreement is observed between the theoretical value (≈ 2.21) and the value obtained through simulation (≈ 2.20), demonstrating that the results properly follow the quadratic dependence of drag on velocity.

This verification reinforces the physical consistency of the numerical modeling, indicating that the aerodynamic behavior of the flow is correctly represented in the adopted computational model.

IX. Conclusions

Based on the Computational Fluid Dynamics (CFD) simulations performed, it is concluded that the Explorer airship exhibits aerodynamic behavior compatible with its intended operational envelope, demonstrating stable flow characteristics and pressure distributions consistent with large-volume configurations. The estimated drag coefficient, on the order of 0.21, is in agreement with values reported in the technical literature for airships of similar scale, indicating aerodynamic efficiency suitable for the proposed mission profile.

The numerical methodology adopted, including the computational domain modeling, mesh criteria, and solution approach, proved to be appropriate for preliminary aerodynamic performance assessments, providing consistent and technically well-founded results. Additionally, the obtained data establish a solid basis for the continuation of the studies, enabling the progressive refinement of the design and its scaling within the context of the Eternaus Program.

As a natural continuation of this stage, it is recommended that complementary analyses be carried out, including investigations under crosswind conditions, transient wake studies for the characterization of vortical structures and potential instabilities, as well as evaluations of geometric modifications aimed at drag reduction and the overall optimization of aerodynamic performance.

Based on the obtained results and the analyses performed, it can be concluded that the aerodynamic drag increase follows, with high accuracy, the quadratic dependence on velocity: $D \propto V^2$ as predicted by theory for incompressible flows. The agreement between the theoretical values and the numerical results indicates that the computational model exhibits a high level of physical consistency, with no evidence of modeling errors, numerical instabilities, or non-physical behavior in the obtained results.

It is also observed that increasing the velocity leads to a more energetic and spatially extended wake, with greater intensity of vortical structures and increased total pressure losses, reflecting higher energy dissipation within the flow. In addition, the contribution of pressure drag becomes more significant, reinforcing the influence of geometry on drag generation. As a consequence, the overall aerodynamic loading increases considerably, directly impacting thrust and power requirements.

From a design perspective, the airship performance demonstrates high sensitivity to operating velocity, particularly in the cruise regime. Small variations in velocity result in significant increases in drag and required power due to the relationships: $D \propto V^2$ and $P \propto V^3$.

Therefore, geometric optimization, especially in the aft region and at the interface with the empennage, proves to be critical for reducing pressure drag and improving the overall aerodynamic efficiency of the vehicle.

Acknowledgments

The authors gratefully acknowledge the Eternaus Aerospace Systems Research Division for supporting this investigation and providing computational resources. Special thanks to the ESSS and ANSYS company for their assistance with the ANSYS Fluent 2025 R2 setup and to the structural analysis group for integrating prestressed geometry data into the aerodynamic model.

References

[1] Jones, R. M., *Buckling of Bars, Plates, and Shells*, Bull Ridge Publishing, Blacksburg, VA, 2006.
[2] Pope, A., and Harper, J. J., *Low-Speed Wind Tunnel Testing*, 3rd ed., Wiley, New York, 1991.
[3] ANSYS Inc., *Fluent Theory Guide, Release 2025 R2*, Canonsburg, PA, 2025.
[4] Menter, F. R., "Two-Equation Eddy-Viscosity Turbulence Models for Engineering Applications," *AIAA Journal*, Vol. 32, No. 8, 1994, pp. 1598–1605. doi:10.2514/3.12149
[5] Schlichting, H., and Gersten, K., *Boundary-Layer Theory*, 9th ed., Springer, Berlin, 2016.
[6] White, F. M., *Viscous Fluid Flow*, 4th ed., McGraw–Hill Education, New York, 2022.
[7] Anderson, John D. JR. Modern compressible flow. 3rd. ed. McGraw-Hill, 2003.
[8] Anderson, John D. Jr. Computational Fluid Dynamics: The Basics with Applications. 1 edition ed. New York: McGraw-Hill Educationl, 1995. v. 206.
[9] Kundu, P. K.; Cohen, I. M.; Dowling, D. R. Fluid Mechanics. 5th. ed.: Academic Press, 2011. 920 p.
[10] Joaquim Junior, C. F.; Cekinski, E.; Nunhez, J. R.; Urenha, L. C. Agitação e Mistura na Indústria. Rio de Janeiro, RJ: Livros Técnicos e Científicos Editora Ltda, 2007. 1 v.
[11] Fletcher, Clive A. J. Computational Techniques for Fluid Dynamics: Specific Techniques for Different Flow Categories: Springer-verlag Berlin Heidelberg, 1988. 2 v.
[12] Arpaci, V. S.; Larsen, P. S. Convection Heat Transfer. Englewood Cliffs, N.J: Prentice-hall, 1984.
[13] Versteeg, H K; Malalasekera, W. An introduction to Computational Fluid Dynamics. 2. ed. United Kingdom: Pearson Education Limited, 2007. 503 p.
[14] Anderson, J. D., Fundamentals of Aerodynamics, 7th ed., McGraw–Hill Education, New York, 2021.
[15] Hoerner, S. F., Fluid-Dynamic Drag: Practical Information on Aerodynamic Drag and Hydrodynamic Resistance, Hoerner Fluid Dynamics, New York, 1965.

.